Bulletin of the Seismological Society of America, Vol. 96, No. 4B, pp. S250–S268, September 2006, doi: 10.1785/0120050811

Thirty-Five-Year Creep Rates for the Creeping Segment of the San Andreas Fault and the Effects of the 2004 Parkfield Earthquake: Constraints from Alignment Arrays, Continuous Global Positioning System, and Creepmeters

by Sarah J. Titus, Charles DeMets, and Basil Tikoff

Abstract We present results from differential Global Positioning System (GPS) surveys of seven alignment arrays and four continuous GPS sites along the creeping segment of the San Andreas fault. Surveys of four alignment arrays from the central creeping segment yield 33- to 36-year average minimum slip rates of 21–26 mm/yr. These rates are consistent with previous alignment array surveys spanning a 10-year period and with rates determined by creepmeters, indicating approximate steady-state creep along the central creeping segment for at least 35 years. Motion between continuous GPS sites that span the central creeping segment is 28.2 ± 0.5 mm/yr for two sites that are 1 km apart and 33.6 ± 1 mm/yr for two sites that are 70 km apart. Slip rates therefore increase with distance from the creeping segment of the San Andreas fault. All rates reported here are significantly slower than the 39 ± 2 mm/yr rate predicted for motion between the Sierra Nevada–Great Valley block and the Pacific plate. Repeat surveys of three alignment arrays following the 2004 Parkfield earthquake demonstrate that its coseismic and short-term postseismic offsets decrease rapidly with distance from the epicenter, from 150 mm to 15 mm to <5 mm at respective distances of 9, 36, and 54 km to the northwest. Continuous GPS data confirm that little coseismic and postseismic slip occurred along the central creeping segment. Geodetic and geologic slip rates are compared and different models for the accommodation of transcurrent deformation across the creeping segment are discussed.

Introduction

The creeping segment of the San Andreas fault is a 175-km-long section of the fault between San Juan Bautista and Cholame (Fig. 1) that separates the locked sections of the fault that ruptured during the Fort Tejon earthquake of 1857 and San Francisco earthquake of 1906. Following the recognition of aseismic creep along this segment of the San Andreas fault (e.g., Tocher, 1960; Allen, 1968; Brown and Wallace, 1968) the U.S. Geological Survey (USGS) made periodic and continuous measurements of creep using alignment arrays (Burford and Harsh, 1980), trilateration networks (Lisowski and Prescott, 1981), and creepmeters (e.g., Schulz *et al.*, 1982; Schulz, 1989) to establish a first-order understanding of the kinematic behavior of the San Andreas fault in central California. These early studies document 30–33 mm/yr maximum creep rates along a 55-km central creeping segment, with rates that decrease to zero slip along northwest and southeast segments toward San Juan Bautista and Cholame, respectively.

The agreement between the rapid creep rates (30–33 mm/yr) for the central creeping segment and a geologic slip rate estimate of 34 ± 3 mm/yr from Wallace Creek (Fig. 1) (Sieh and Jahns, 1984), imply that little or no interseismic frictional locking occurs on the creeping segment. We therefore installed a Global Positioning System (GPS) network, including four continuous GPS stations (Fig. 1), across the central creeping segment hoping to separate the components of discrete and distributed deformation flanking a major strike slip without the strong interseismic elastic overprint that would normally complicate any attempt to isolate the off-fault deformation. During this work, we found a well-preserved alignment array that had accumulated approximately 1 m of offset since its installation in the late 1960s. After discovering that most alignment arrays along the creeping segment had not been surveyed for more than two decades except near Parkfield (Baker, 1993), we located and resurveyed seven alignment arrays to estimate average ~35-year creep rates that complement our continuous GPS creep rates. Our data indicate less agreement than previous studies between modern geodetic creep rates and geologic

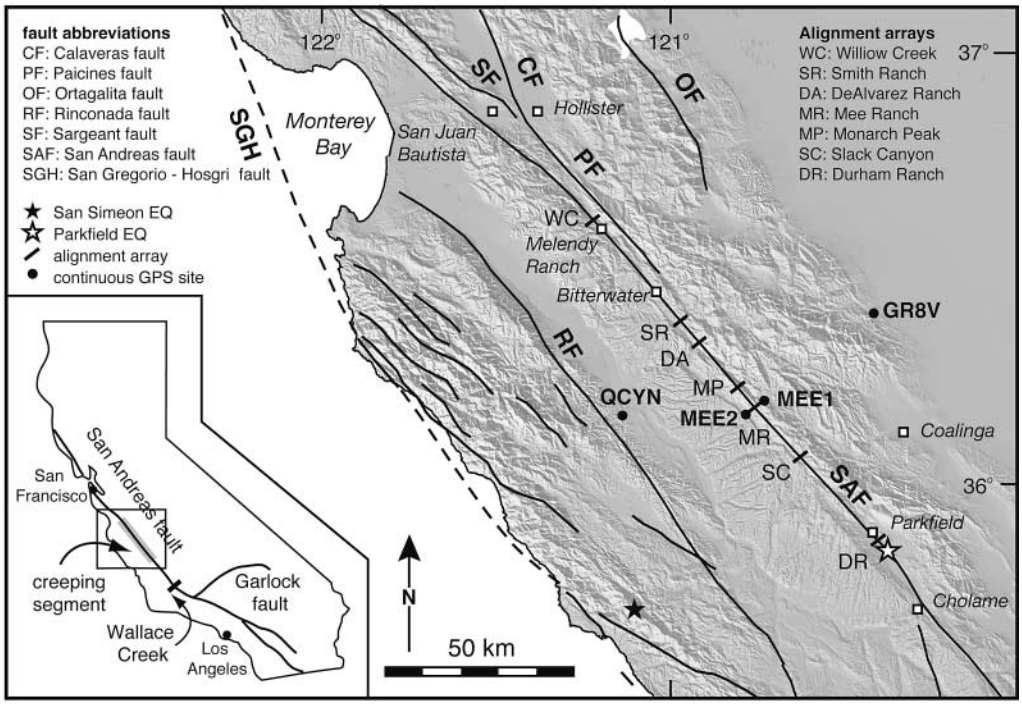

Figure 1. Map of central California showing the location of alignment arrays and continuous GPS stations along the creeping segment (between San Juan Bautista and Cholame) of the San Andreas fault. The epicenters of the San Simeon and Parkfield earthquakes are also shown. Map inset indicates locations of major features within California, discussed in text.

slip rates, suggesting more complicated accommodation of transcurrent deformation across the creeping segment.

In this article, we describe our methodology for differential GPS surveys of alignment arrays in detail. Using differential GPS alignment array surveys and continuous GPS data, we expand on and reinforce evidence presented by Titus *et al.* (2005) for modern surficial creep rates that are slower than the widely accepted geologic slip rate of 34 mm/yr. We also document the kinematic response of the creeping segment to nearby earthquakes, demonstrating that the magnitude of coseismic and postseismic slip triggered by the Parkfield earthquake decreases drastically along the central creeping segment. Finally, we compare short- and long-term creep rates both along and across the creeping segment and present two models that integrate modern creep rates with geologic slip rates to account for the distribution of transcurrent motion across the San Andreas fault system.

Alignment array surveys

Original Surveys: 1969–1979

In the late 1960s, the USGS installed 25 alignment arrays along the creeping segment of the San Andreas fault, each consisting of 8–20 benchmarks oriented approximately perpendicular to the active trace of the San Andreas fault and ranging in length from 30 to 200 m (Burford and Harsh, 1980). Each monument is a standard USGS brass benchmark set in a concrete posthole or inside a transite pipe (Fig. 2). Alignment array locations were established near the midpoints of single *en echelon* segments of the fault based on mapping by Brown (1970) in order to avoid areas where creep might be partitioned onto different fault strands. Each alignment array was designed for surveys with a theodolite, with one instrument station, two end stations, and several deflection stations (Fig. 2) (Lienkaemper *et al.*, 2006).

The deformation that accrues across an alignment array can result from a combination of discrete fault slip between two rigid blocks and distributed shearing as illustrated in Figure 3. Although the monument endpoints in each of the scenarios in Figure 3 are the same, the displacements experienced by each monument vary depending on how deformation is accommodated (discrete or distributed), as well as on the initial orientation of the array with respect to the fault. Discriminating between the alternative models for deformation thus requires knowledge of the precise initial and final coordinates of each array monument with respect to some common external reference point.

Monuments were surveyed multiple times over a 10-year period to document creep rates along the active trace of the creeping segment (Burford and Harsh, 1980). Deflection stations were used to determine the lateral separation between two least-squares-fit lines at their intersection along the San Andreas fault (Fig. 2). Because this best-fit estimate of the creep rate is based on the position of multiple monu-

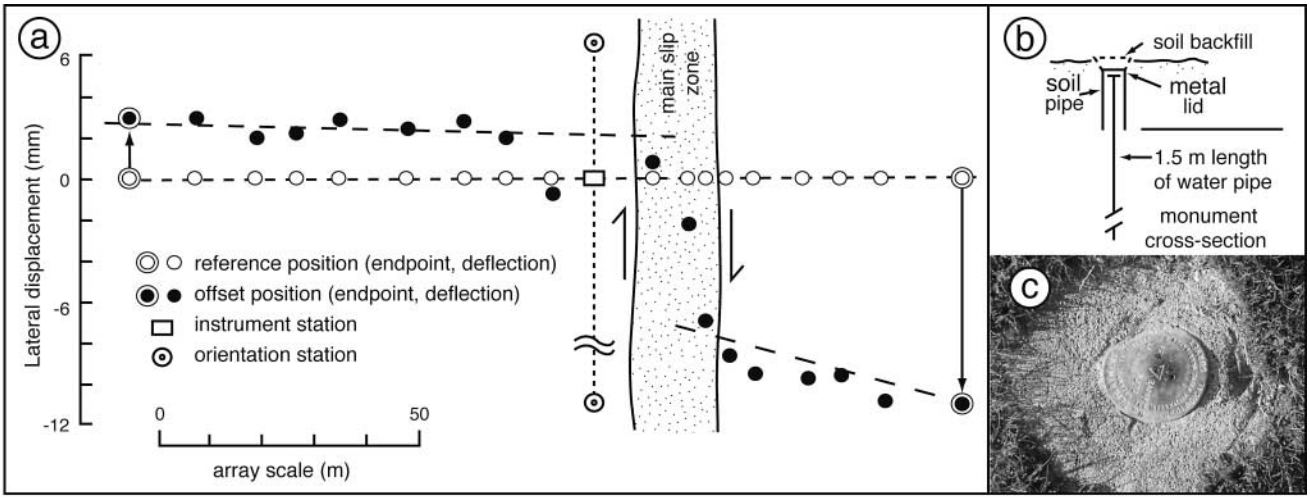

Figure 2. (a) Schematic map of an alignment array with instrument, orientation, endpoint, and deflection stations used in theodolite surveys of alignment arrays. Dashed lines show the linear regression through the deflection stations used for best-fit analysis. Arrows at endpoint stations indicate displacements for endpoint analysis. Examples of monuments are shown by (b) the cross-section cartoon and (c) plan-view photograph. Modified from Burford and Harsh (1980).

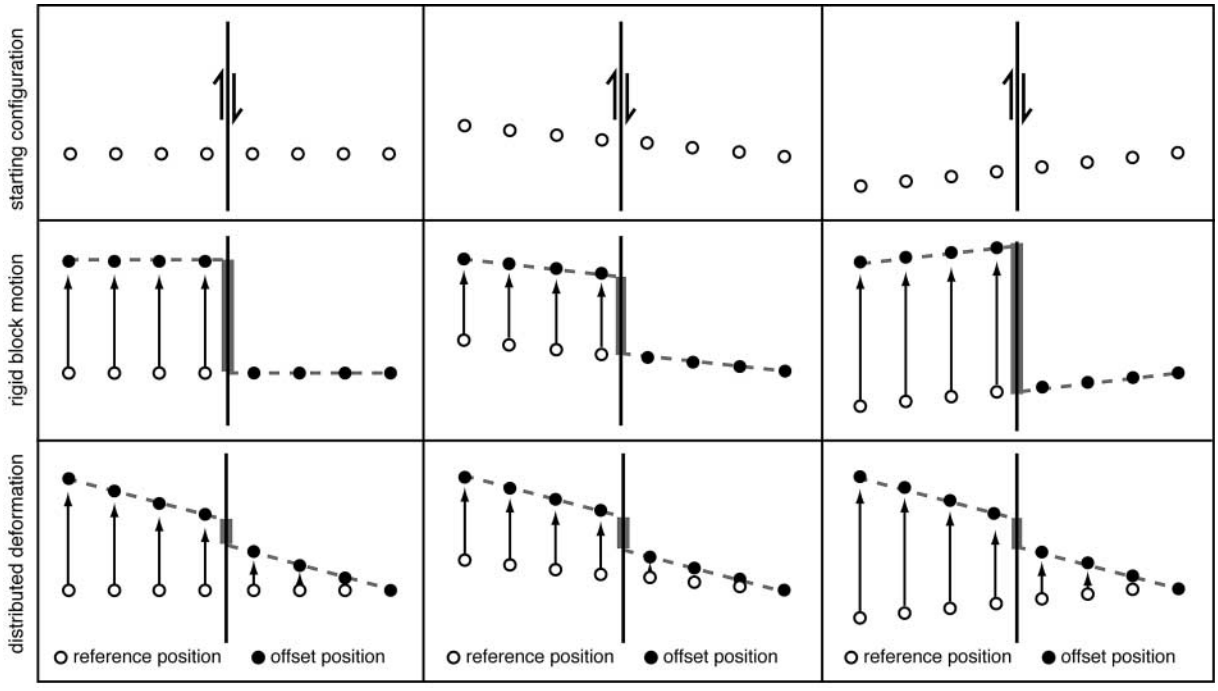

Figure 3. Cartoons illustrating alignment array monuments with different starting configurations (first row) displaced to their final positions by block motion (second row) and primarily by distributed deformation (third row). The rightmost monument is fixed in all scenarios and the final fault-parallel distance between the two endpoints is also the same. The thick, vertical gray bar represents the magnitude of discrete deformation. Without knowing the precise starting geometry, the same ending geometry could be observed but caused by different displacement fields.

ments, it is generally insensitive to irregular displacement patterns and typically represents a minimum estimate of discrete fault slip. Displacement of the end stations was used to derive an endpoint rate that represents both the discrete and distributed offset accommodated across the alignment array.

Figure 4a shows three examples of monument displacements between theodolite surveys as well as the typical scatter observed in monument positions. Repeatability analysis of theodolite surveys suggests a standard deviation of approximately ± 0.4 mm for the location of each monument (Burford and Harsh, 1980). Galehouse and Lienkaemper (2003), however, suggest a more conservative 1- to 2-mm estimate for alignment station location errors based on a random walk assumption (Langbein and Johnson, 1997).

Differential GPS Methodology

In 2003 and 2004, we assessed the condition of the USGS alignment arrays along the central creeping segment and surveyed seven arrays with two or more intact monuments on each side of the fault. In addition to the seven arrays reported here, we visited but could not locate the following alignment arrays: Cross-Willow, Melendy Ranch, Pinnacles, Dry Lake, Eade Ranch, and Water Tank (table 1 of Burford and Harsh, [1980]).

For our alignment array surveys, we used differential GPS measurements instead of theodolites for two reasons. First, GPS technology and data analysis software are ubiquitous and thus establish a basis for future work. Second, differential GPS techniques allow for unambiguous determination of horizontal and vertical deformation near the fault and facilitate ties to an external reference frame if required.

During a given survey, each monument was occupied for a minimum of 20–30 min and up to 24 hr with a dual-frequency Trimble 5700 and a Zephyr geodetic antenna. Trimble's GPSurvey software (www.trimble.com) was used to determine the relative location of each marker with respect to a continuously operating GPS receiver along or near the array. A repeatability analysis of relative site locations for consecutive 20-min intervals (Fig. 5) indicates that the north and east baseline components are consistent at the ± 2.5 mm level (1σ) and vertical component at the ± 5 mm level (1σ),

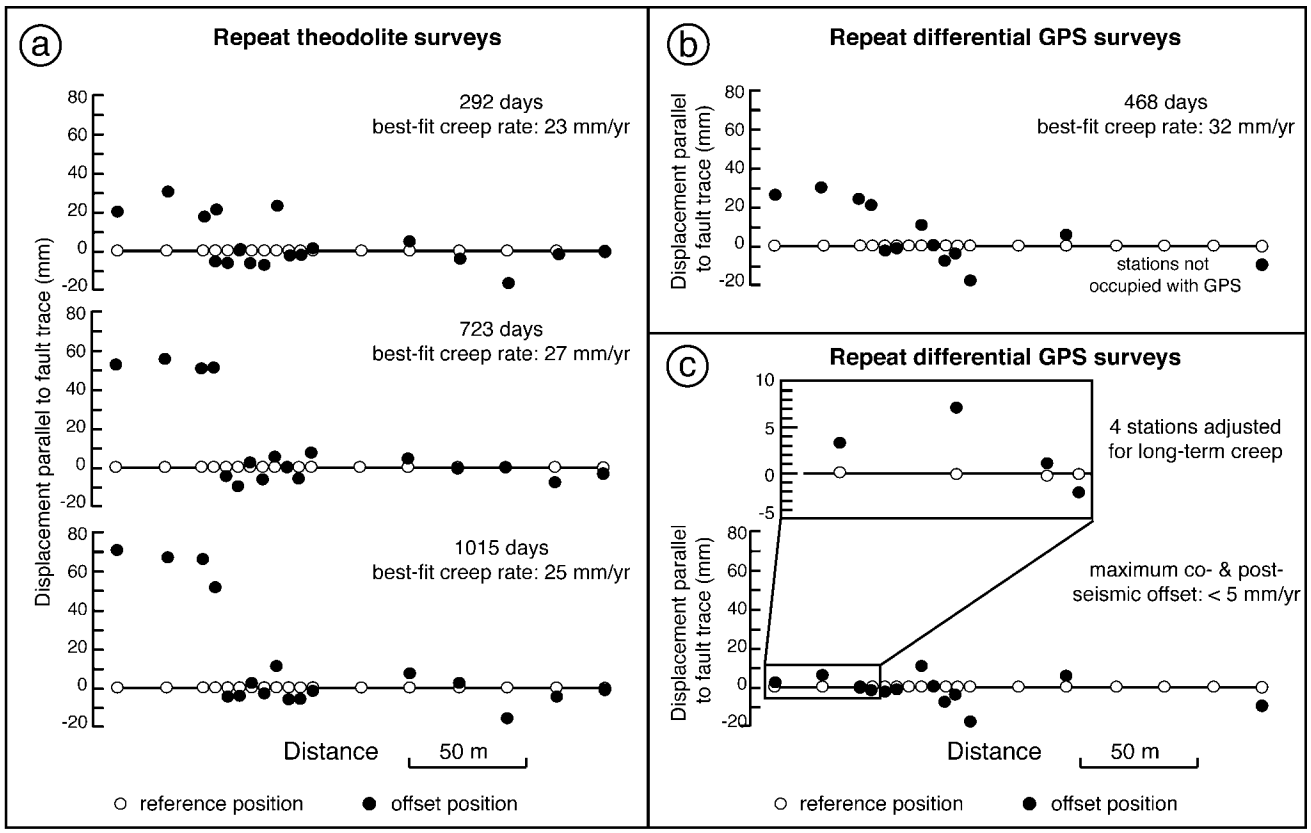

Figure 4. (a) Three examples of fault-parallel, incremental displacements measured from theodolite surveys of the Mee Ranch alignment array (Burford's original notes). Scatter of monument positions relative to best linear fits is typically 5–10 mm. Incremental displacements between our two differential GPS surveys of the Mee Ranch alignment array are shown in (b) and (c). (b) No corrections for long-term creep were made; (c) the four Pacific plate monuments were adjusted for long-term creep at a rate of 24 mm/yr.

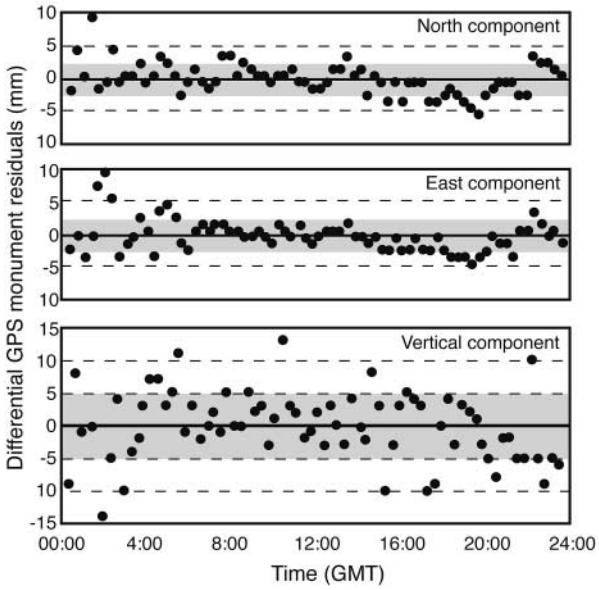

Figure 5. Repeatability analysis for the north, east, and vertical components of two GPS stations (MEE1 and MEE2) processed using Trimble's GPSurvey software. The zero line in each plot indicates the average north, east, and vertical distances between MEE1 and MEE2, and the data points show the residual from this average for consecutive 20-min intervals. The data span a single 24-hr day for the two continuous GPS stations, which are separated by 1025 m horizontally and 114 m vertically. Gray boxes indicate the standard deviation for these residuals at the 1σ level.

comparable to precisions reported by Genrich and Bock (1992).

The theodolite-based measurements reported by Burford and Harsh (1980) and our differential GPS measurements unfortunately use different points of reference, whose locations with respect to each other are unknown. It is thus impossible to use a combination of the original theodolite data and our GPS observations to reconstruct the movements of individual monuments relative to a common reference point. This constraint effectively restricts our analysis to the determination of best-fit creep rates and not endpoint creep rates, as described in more detail in the following section.

Differential GPS Best-Fit Creep Rates

With a few simplifying assumptions, we are able to construct useful, best-fit estimates of fault creep for each array using only the differential GPS measurements. We assume that the original monuments in the alignment array were colinear and have been offset over time by the San Andreas fault. The offset of the two lines that best fit the monuments on either side of the fault should represent a relatively accurate estimate of the discrete fault-induced offset, provided that any additional motion of the markers caused by nontectonic processes such as soil creep and slope instability is dominantly random and largely uncorrelated between adjacent markers.

Before inverting the GPS-derived monument locations to compute their best-fitting lines, we transformed the north and east monument coordinates and their uncertainties into a fault-centered coordinate system in which the coordinate axes are oriented parallel and orthogonal to the local strike of the fault (Table 1). The north and east monument locations relative to our reference point for each alignment array were thus reexpressed as fault-parallel and fault-orthogonal distances. A linear inversion of the transformed monument coordinates weighted by their transformed variances and covariances yielded least-squares estimates of the lines that fit the monument coordinates on both sides of the fault. The fault offset is determined from the intersection of these two best-fit lines at the inferred position of the fault (Fig. 2). Because best-fit rates only capture the magnitude of discrete offset along the fault, they represent minimum estimates of fault creep. The results from these inversions are presented in the following section.

Multiple sources of error can affect the estimated fault offsets and hence creep rates. Rotation of the monument coordinates into a fault-centered coordinate system can contribute to small errors in the best-fit rates, as illustrated in Figure 6. Incorrect determination of the local strike of the San Andreas fault and the strike we assume for our coordinate transformation will introduce an error into our estimate of the fault offset proportional to the cosine of the angle between the correct azimuth and the azimuth we employ (Fig. 6a). Fortunately, for a plausible range of angular differences, $-10^\circ < \alpha < 10^\circ$ (Fig. 6b), the creep rate is underestimated by only 1.5%.

The best-fitting lines and fault offsets become increasingly sensitive to random or systematic noise in individual monument locations as the number of monuments that are available on one or both sides of the fault decreases. This is of particular concern for two arrays we surveyed (DeAlvarez Ranch and Willow Creek), where there are only two monuments on one side of the fault.

If nontectonic site movement is not random over time, as we assume, and instead is correlated between adjacent sites, our measurement uncertainty also increases. For example, coordinated movement of two or more adjacent monuments via downslope soil creep can mimic fault slip, particularly if a significant component of that motion is parallel to the local fault trace. The assumption of monument colinearity is also not technically correct, as original monument positions vary by 3 cm with an root mean square scatter of approximately 9 mm (J. Langbein, personal comm., 2005). However, this scatter combined with monument wander and averaged over 30 years does not significantly affect the long-term creep rates.

It is difficult to incorporate these sources of error into our analysis. We therefore attempt to estimate realistic uncertainties via sensitivity tests that employ different data subsets for individual arrays. We also compare results from

Table 1
Alignment Array Information

Site Name	ID	Latitude (°N)	Longitude (°W)	Length (m)	SZW*	Fault Azimuth†	Array Azimuth†	Survey Dates DFS‡	Survey Dates DLS‡	Survey Dates This Study	Slip Rates (mm/yr)§ BF	Slip Rates (mm/yr)§ EP	Slip Rates (mm/yr)§ This Study
Willow Creek	WC	36.5950	121.1850	75	≤13	N37W	N41E	67:272	77:025	04:099	26.4	22.7	20.2
Smith Ranch	SR	36.3833	120.9693	120	≤6	N36W	N54.5E	70:225	71:217	03:299	22.1	33.3	26.2
DeAlvarez Ranch	DA	36.3167	120.9017	138	≤15	N35W	N49E	70:225	77:236	04:101	22.5	31.4	24.0
Monarch Peak	MP	36.2133	120.7983	96	≤18	N35W	N54E	68:044	77:041	04:102	16.0	17.3	17.4
Mee Ranch	MR	36.1800	120.7567	200	≤5	N36W	N61E	70:238	77:235	03:299	26.5	26.0	23.7
										04:339	—	—	23.0
Slack Canyon	SC	36.0650	120.6283	79	≤6	N40W	N53E	68:045	79:130	03:300	23.9	30.0	21.2
										04:346	—	—	23.0
Durham Ranch	DR	35.8850	120.4217	32	≤9	N41W	N52.5E	68:046	79:118	04:076	13.1	14.6	8.7
										04:359	—	—	13.3

We surveyed the Mee Ranch, Slack Canyon, and Durham Ranch alignment arrays both before and after the 2004 Parkfield earthquake and each survey has a corresponding row in the table. The slip rates quoted for the second survey of these three arrays reflect the long-term creep rate as well as any coseismic or postseismic offsets due to the earthquake.

*SZW, apparent slip-zone width.

†Fault and array azimuths from Burford's original notes.

‡DFS and DLS, dates of first survey and last survey (Burford and Harsh, 1980), respectively given as year: Julian day.

§The best-fit (BF) and endpoint rates (EP) of Burford and Harsh (1980) and our best-fit creep rates are reported.

the seven arrays with other measures of fault creep to establish the overall consistency and hence reliability of the best-fit creep rates described in the following section.

Differential GPS Endpoint Creep Rates

In theodolite surveys of alignment arrays, endpoint rates are used to document the distributed component of deformation captured by the array (Fig. 3) (see also Lienkaemper *et al.*, [2006]). The methodology described previously for our differential GPS data, where monument positions are rotated into a fault-parallel framework, does not yield accurate endpoint creep rate estimates, as is erroneously reported by Titus *et al.* (2005). Because the end points are frequently located far (tens of meters) from the fault, even small errors (<1°) in the estimated orientation of the fault will translate into fault-parallel endpoint offsets that vary by several orders of magnitude (Fig. 6c). In addition, estimation and interpretation of endpoint offsets depends on the original orientation of the alignment array with respect to the fault (Fig. 3). Overcoming these problems will require locating and occupying any surviving original alignment array reference marks with GPS, such that the original and present locations of the individual monuments can be specified relative to a common reference point.

Results from Alignment Array Surveys

Results from the differential GPS alignment array surveys are shown in Figure 7. Each array shows one clearly defined offset, ranging from ~25 to 100 cm, that corresponds to offset along the actively creeping trace of the San Andreas fault. The estimated fault offsets are an order of magnitude greater than the typical monument deviations from the best-fit line (40–60 mm), indicating that the underlying creep rates can be determined to within a few percent. The monument residuals are often greater than the ~5 mm precision with which we can locate monuments using differential GPS. The absence of obvious patterns in the residuals suggest that random wander of monuments due to changes in precipitation, slope stability, and soil creep dominates the noise.

Creep rates determined from the differential GPS surveys are presented in Table 1, together with 10-year rates from theodolite surveys. These rates can also be compared to rates derived from creepmeters in Table 2 (described in more detail in a later section). Details pertinent to the individual alignment arrays are discussed next.

Willow Creek and DeAlvarez Ranch Arrays. Both arrays have only two monuments on the northeast side of the fault. In each case, the monument closest to the fault on its northeast side exhibits the least offset, thereby implying that the creep rate determined from a best-fit analysis could be too slow. We attempted to derive a more robust estimate of the offset for each array by averaging the fault-parallel locations of the two monuments instead of extrapolating the line that best fits the two monuments to the fault location. Our ~30-year creep rates for both arrays are slower than the short-term rates. The creep rate at Willow Creek, however, is slightly faster than creep rates from nearby creepmeters at Willow Creek and Melendy Ranch. Data sensitivity tests suggest approximate standard errors in the rates for both sites of ±2 mm/yr.

Smith Ranch Array. This well-preserved array yields the most robust and fastest long-term slip rate for any of the arrays we surveyed. Inversions of different subsets of the 16

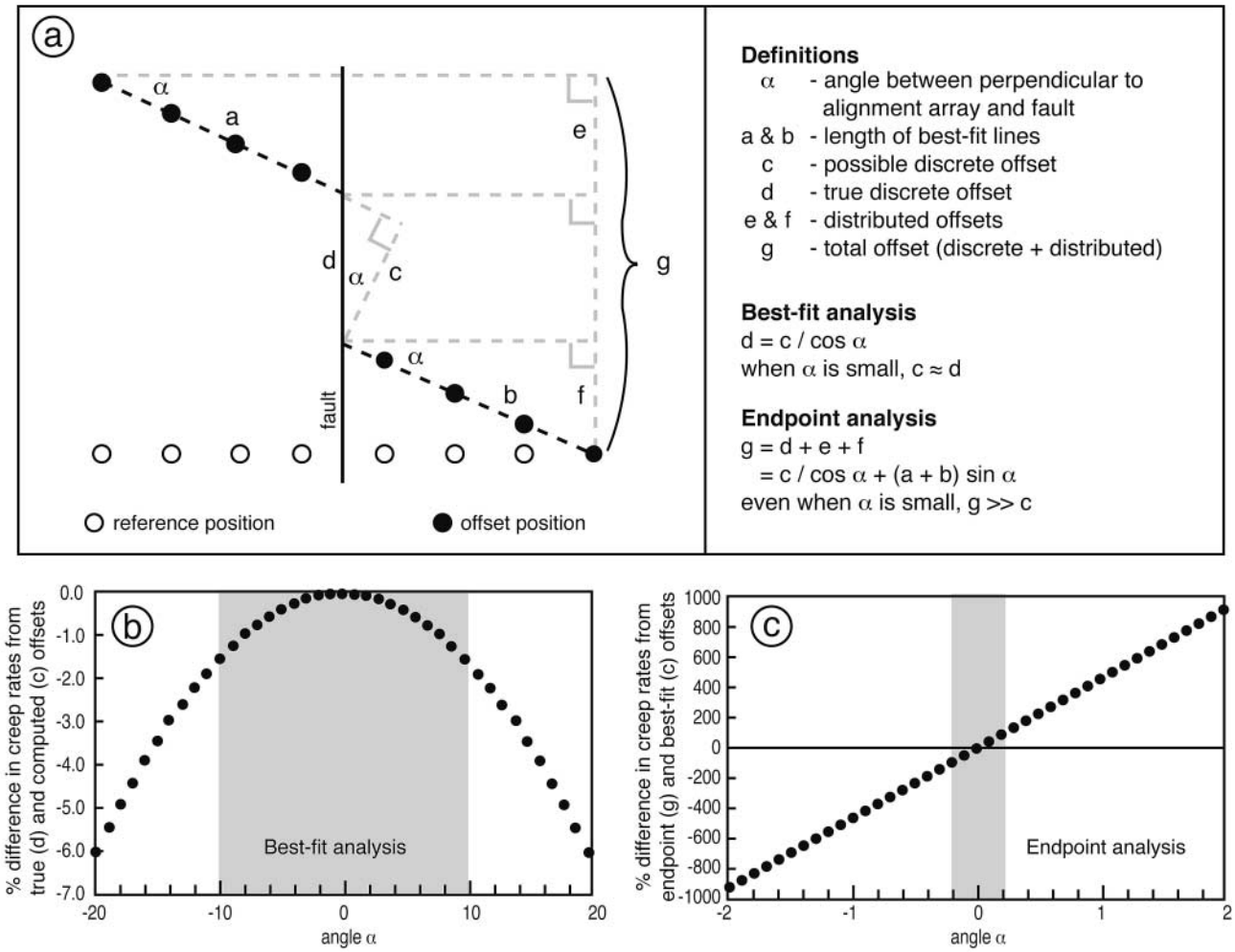

Figure 6. (a) Diagram of reference and offset positions of alignment array monuments demonstrating the geometric relations between the true discrete offset along the fault (quantity d) and offset computed when the original alignment array orientation is not precisely known (quantity c). The distributed offset is captured by looking at the position of the endpoints. Panels (b) and (c) show the effects the angle α on creep rate estimates for best-fit and endpoint analyses, respectively. The gray bar in (b) demonstrates that for $\alpha \pm 10°$, creep rate errors are quite low. The gray bar in (c) shows that geologically reasonable creep rates (comparable to those determined by best-fit rates) are only obtained for $\alpha \pm 0.2°$.

monuments in this array to determine the sensitivity of the estimated creep rate suggests an uncertainty of less than ± 0.5 mm/yr in our best estimate of 26.2 mm/yr. Our best-fit rate lies approximately midway between previous best-fit and endpoint estimates of 22.1 mm/yr and 33.3 mm/yr but agrees well with the creepmeter rate of 26.5 mm/yr based on data collected from 1969 to 1980.

Mee Ranch Array. With 14 monuments distributed along its length, the Mee Ranch alignment array yields a well-constrained minimum creep rate of 23.7 mm/yr over the past 33 years. Based on sensitivity tests using subsets of the data, we estimate a realistic standard error of ± 1 mm/yr. This 33-year-average rate is roughly 10% slower than the 7-year average rate of 26.5 mm/yr.

Monarch Peak Array. Despite its central location along the creeping segment, creep rates at Monarch Peak have been consistently slower than other locations along the central creeping segment (Burford and Harsh, 1980; Schulz *et al.*, 1982). Rymer *et al.* (1984) attribute slower creep at this site to partitioning of slip onto other active strands of the San Andreas fault, and not to distributed deformation outside the alignment array. Our 36-year-average rate at this location, 17.4 $\pm$ 0.5 mm/yr, is similar to the 9-year alignment array creep rate of 16.0 mm/yr and an 11-year creepmeter rate of 15.0 mm/yr.

Slack Canyon Array. This relatively short alignment array has only eight monuments. The 35-year-average slip rate of 21.2 mm/yr is slower than previous estimates of both best

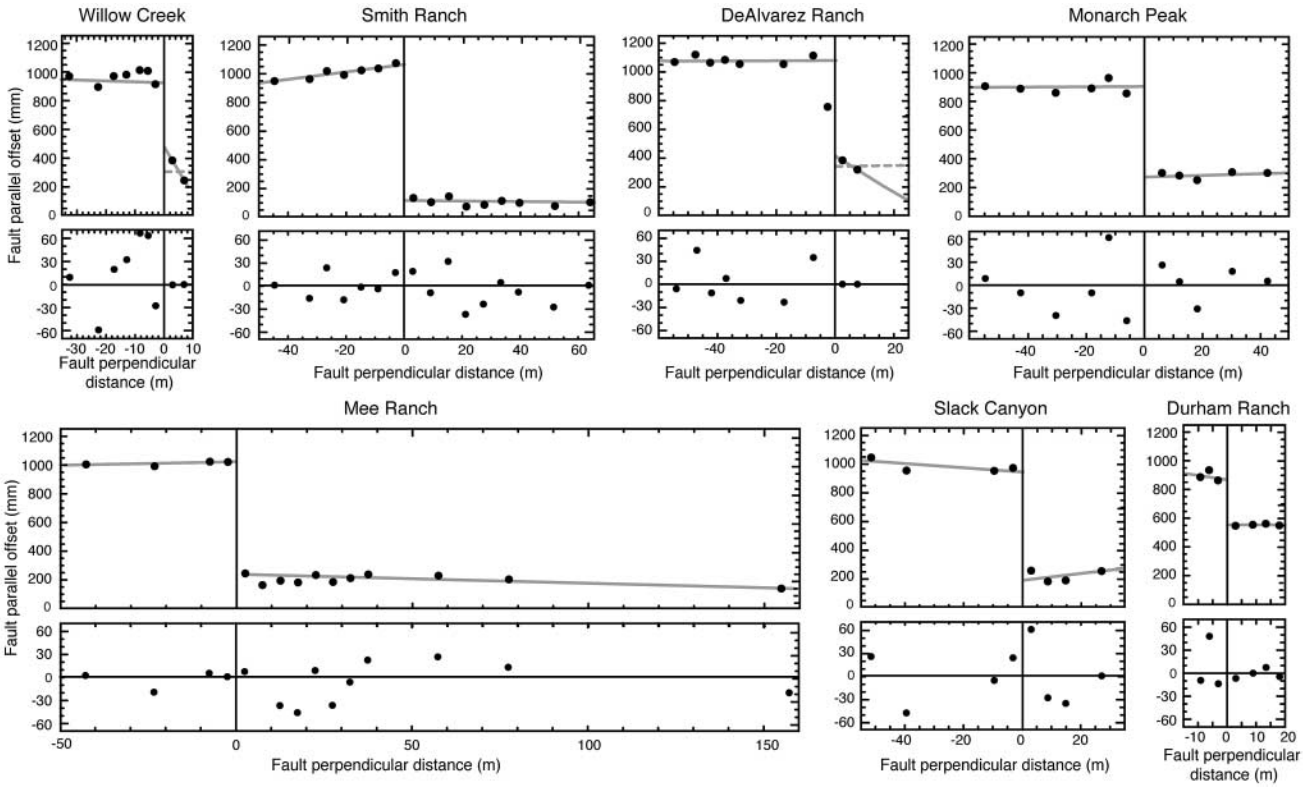

Figure 7. Results from differential GPS surveys of seven alignment arrays. Upper panels show monument locations rotated into a local fault-parallel (vertical line) coordinate system. Pacific plate monuments are always on the left side of the fault, and best-fit lines are shown for monuments on either side of the fault. Fault-parallel monument locations are arbitrary (position along the *y*-axis). The lower panels show monument residuals relative to best-fit lines. The horizontal and vertical scales are the same scale for all alignment arrays.

Table 2
Creepmeter Information

Name	Site	Distance (km)	Installation Date	Discontinued Date	Creep Rate (mm/yr) 1980	Creep Rate (mm/yr) 2004
Willow Creek	WLC1	39	Oct. 1972	?	14.3	NA
Melendy Ranch	XMR1	40	June 1969	—	19.0	17.6
Bitterwater	BIT1	68	July 196?	Oct. 1988	16.9	—
Smith Ranch	XSR1	70	June 1969	May 1982	26.5	—
Monarch Peak	XMP1	94	June 1969	Aug. 1983	15.0	—
Slack Canyon	XSC1	117	June 1969	—	23.5	20.8
Taylor Ranch	XTA1	144	Oct. 1985	—	—	9.3
Durham Ranch	XDR1	145	July 1969	Oct. 1985	10.5	—

Distances are relative to creepmeter XSJ2 in San Juan Bautista. All reported creep rates are endpoint rates (simple averages of total offset divided by time). Rates from 1980 are from Schulz *et al.* (1982), and 2004 rates are based on offsets from the time of installation up to the Parkfield earthquake from USGS data available at http://quake.wr.usgs.gov/research/deformation/monitoring.

fit and endpoint but agrees remarkably well with a 20.8 mm/yr creep rate determined from 35 years of creepmeter measurements at this location (Table 2). Sensitivity analyses and the excellent agreement with the independently measured creepmeter rate for 1970–2004 suggest the standard error in the best-fit rate is ± 1 mm/yr.

Durham Ranch Array. The short Durham Ranch array also has only eight monuments, some of which were covered by several centimeters of soil that had to be removed prior to our survey. As a consequence, the rate we estimate from our survey is less certain than for the other arrays. Over the past 36 years, our results indicate that creep averaged 8.7 ±

1 mm/yr, the slowest of the arrays surveyed. This rate agrees well with the 9.3 mm/yr creep rate from the nearby Taylor Ranch creepmeter for 1985–2004, but is slower than earlier alignment array and creepmeter rates at the Durham Ranch.

Continuous GPS Results

Four GPS stations flank the creeping segment (Fig. 1) and provide useful independent measures of deformation across the creeping segment at a scale larger than that captured by alignment arrays. The two stations southwest (QCYN and MEE2) and northeast (MEE1 and GR8V) of the fault were installed in local bedrock with dual-frequency Trimble 4700s or 5700s with Zephyr geodetic antennas.

Continuous code-phase GPS measurements are processed using GIPSY analysis software (Zumberge *et al.*, 1997), precise satellite orbits and clocks from the Jet Propulsion Laboratory (Pasadena, California), and a point-positioning analysis strategy that includes resolution of phase ambiguities. Daily station coordinates are estimated in a nofiducial reference frame (Heflin *et al.*, 1992) and then transformed into ITRF2000 (Altamimi *et al.*, 2002). Regional interstation correlated noise is estimated from these and numerous other continuous GPS time series from the western United States using a procedure described by Marquez-Azua and DeMets (2003). This common mode noise is removed from the coordinate time series, resulting in time series dominated by linear tectonic motion, seismic offsets and transient signals from nearby earthquakes, site-specific noise, and residual common-mode noise.

Because this article is concerned with both the relative slip across the creeping segment at different spatial scales and with coseismic and postseismic deformation along the creeping segment associated with nearby earthquakes, two reference frames are used to examine the GPS coordinate time series for the four stations considered here. The coseismic and postseismic responses of the four sites are examined relative to the Sierra Nevada–Great Valley block (Fig. 8a,b), which is a natural external reference frame for interpreting geodetic velocities along the creeping segment. Motion of the Sierra Nevada–Great Valley block relative to ITRF2000 is specified using an angular velocity vector (11.7° S, 63.9° E, 0.455°/m.y.) that best fits the velocities of 11 continuous GPS sites found within the block boundaries, as defined by Dixon *et al.* (2000). In contrast, slip on the creeping segment is examined by specifying the relative motions of pairs of sites (i.e., MEE1–MEE2 and GR8V–QCYN) holding one site fixed, and not relative to an external reference frame (Fig. 8c).

Figure 8 shows the coordinate time series of each site relative to the Sierra Nevada–Great Valley block. All four sites exhibit clear elastic responses to the 22 December 2003 San Simeon earthquake. The elastic response of the site farthest from the epicenter, GR8V, is smaller than for the remaining three sites, as expected for a regional-scale elastic response. The southward-directed coseismic offsets exhibited by the north components (Fig. 8a) significantly exceed the small or zero offsets exhibited by the east components (Fig. 8b), indicating that all four sites moved largely southward during the earthquake. Variations in the apparent preseismic and postseismic motions at all four sites (Fig. 8a) are strongly in phase with the common-mode noise we removed from their coordinate time series, indicating that imperfectly estimated common-mode noise is likely to be responsible for most of the apparent variations in motion, as opposed to preseismic and postseismic transient processes. Careful examination of the differential motions of the two site pairs (Fig. 8c) suggests that all apparent variations, including the apparent slowing of motion between the site pairs just before and after the San Simeon earthquake, occur annually (see for example the similar slowing of motion for both site pairs that occurs in late 2004 and early 2005). To first order, we therefore interpret the motions of all four sites as linear in time, with step offsets coinciding with the 22 December 2003 earthquake.

The coseismic offsets at the four sites during the 28 September 2004 Parkfield earthquake are 5 mm or less in both the north and east components (Fig. 8a,b). Estimating the precise coseismic motions is complicated by incompletely removed common-mode noise in the time series, which appears clearly in both components of all four time series in the months after the earthquake. Formal inversions of the time series that compare the 5-day average site locations before and after the earthquake demonstrate that none of the sites moved more than several millimeters, thereby indicating that the regional elastic response was small or zero at these sites. Moreover, the obvious lack of differential motion between sites MEE1 and MEE2 coinciding with or following the earthquake (Fig. 8c) clearly shows that the Parkfield earthquake did not trigger measurable coseismic slip or postseismic creep along this part of the central creeping segment.

We estimated the 3-year-average motions of these sites via a formal inversion of the individual coordinate time series that allows for instantaneous station offsets during the 2003 San Simeon and 2004 Parkfield earthquakes and downweighting of the observations for 3 months after each earthquake to allow for possible postseismic transient motions.

Relative to site MEE1, MEE2 moves 28.2 ± 0.5 mm/yr toward N40°W ± 1°, several degrees counterclockwise from the estimated orientation of the San Andreas fault at the Mee Ranch (N36°W, Table 1) and the N35°W ± 1° motion of the Pacific plate relative to the Sierra Nevada–Great Valley block predicted for this location. This rate is insignificantly different from that reported by Titus *et al.* (2005). The coseismic and postseismic responses of these sites to the Parkfield and San Simeon earthquakes, as well as the common-mode components of noise in the coordinate time series, are identical because of the relative proximity of these sites, and therefore cancel when the site motions are differenced (Fig. 8c). Their relative motions are thus well determined

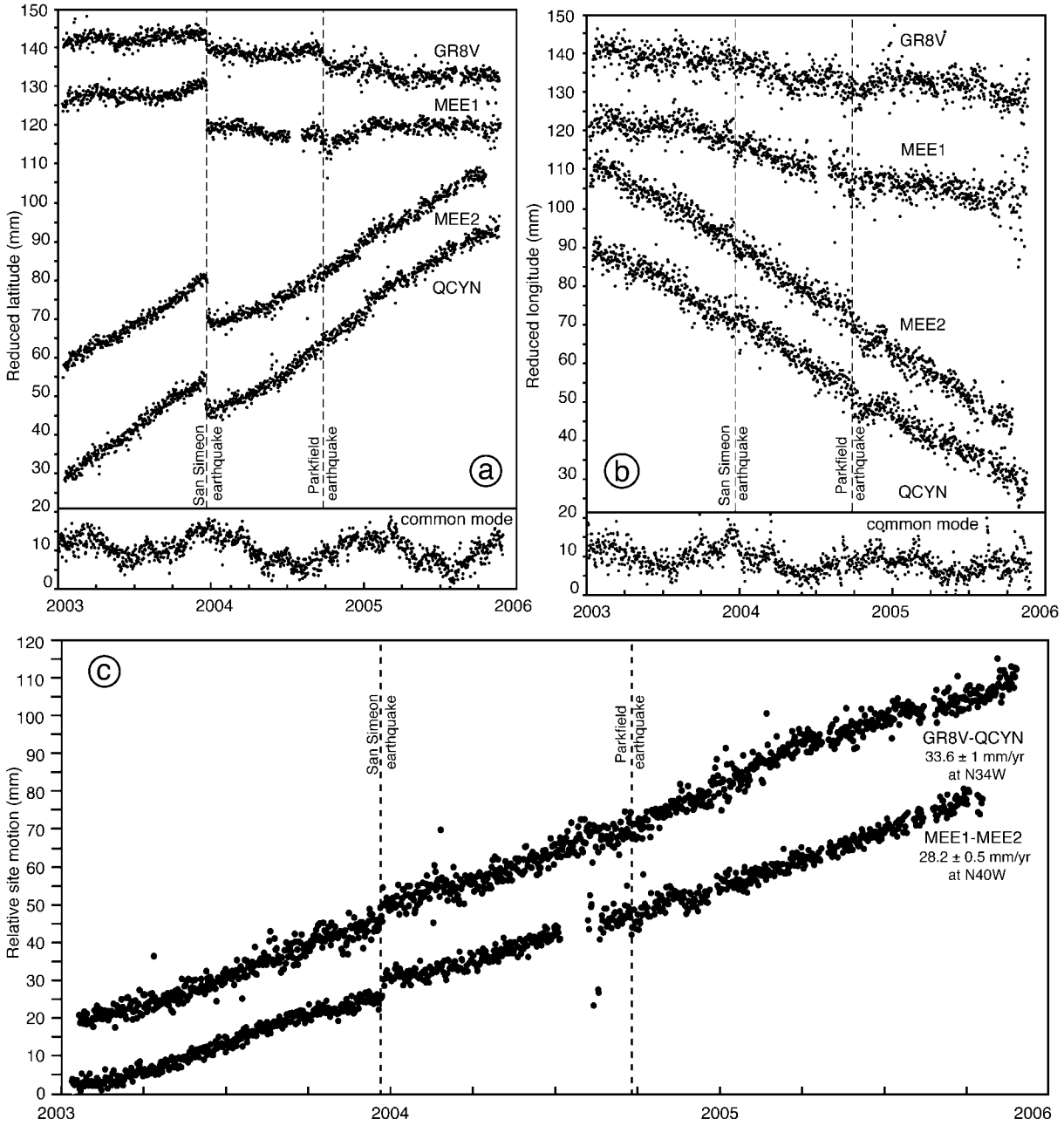

Figure 8. (a) North and (b) east component of coordinate time series for continuous GPS sites relative to the Sierra Nevada–Great Valley block. All site coordinates have been corrected for common-mode noise, an example (from MEE1) of which is shown at the base of each panel. (c) Relative site motions for MEE1-MEE2 and GR8V-QCYN after correcting individual sites for coseismic and postseismic motions and not relative to an external reference frame.

despite disruption of the individual site time series by the Parkfield and San Simeon earthquakes.

Relative to site GR8V, QCYN moves approximately 33.6 ± 1 mm/yr toward N34°W (Fig. 8c), parallel within uncertainties to the predicted direction for Sierra Nevada–Great Valley motion relative to the Pacific plate. This rate significantly exceeds the 30 ± 2 mm/yr rate averaged over 17 months reported by Titus *et al.* (2005). Whether this difference is real or is instead caused by uncertainties in estimating and correcting for the disrupting effects of the San Simeon and Parkfield earthquakes is unclear. Unlike sites MEE1 and MEE2, neither the coseismic responses, postseismic responses, nor common-mode noises of GR8V and QCYN, which are 70 km apart, are identical. These re-

sponses, therefore, cancel less effectively in a calculation of their relative site motions, thereby increasing the uncertainty of this measurement.

Variations in Fault-Parallel and Fault-Perpendicular Creep Rates

Figure 9 summarizes slip rates from this and previously published work as a function of distance along the trace of the San Andreas fault. Rates are discussed in more detail below for near-field, intermediate, and far-field distances across the San Andreas fault. The pattern from each scale of observation is similar, with the highest creep rates along the central creeping segment and decreasing rates toward the locked segments of the fault to the northwest and southeast. The average creep rates at each scale are consistent with a gradient of increasing rates of deformation at increasing distances perpendicular to the San Andreas fault.

Nearfield Rates

Measures of creep using instruments located within ± 10 m of the fault come from creepmeters and the best-fit creep rates recorded by alignment arrays (Fig. 9a). Creepmeter data have been collected from the creeping segment since ~1970, spanning approximately the same interval as our alignment array surveys. To first order, the cross-fault displacements along the central creeping section (XMR1, BIT1, XSR2, and XSC1 in Fig. 10) accumulate steadily and thus are useful for estimating long-term creep rates.

The average creep rates are endpoint rates, computed by dividing the total offset by the time interval in question (e.g., Schulz *et al.*, 1982; Schulz, 1989). Random walk of the anchor points (e.g., Langbein and Johnson, 1997), the effects of changes in precipitation and seasonal variations (e.g., Roeloffs, 2001), and tectonically induced variations in creep rates are ignored in our simplistic analysis and are assumed to average down to insignificant levels over the long time spans considered here. Creep rates for select creepmeters on 10- to 30-year timescales are reported in Table 2. The close agreement between the rates measured by creepmeters and alignment arrays (Table 1) strongly indicates that these rates are good measures of the discrete offset within ± 10 m across the San Andreas fault. The average rate at this scale of observation is 25 ± 1 mm/yr for the central creeping segment.

Intermediate Distance Rates

Measures of fault creep at intermediate distances from the San Andreas fault, defined here to be distances of 10 m to 1 km, are derived from alignment array endpoint rates, short-range trilateration networks, and the relative motion between continuous GPS stations MEE1 and MEE2 (Fig. 9b).

For alignment array measurements, endpoint rates are faster than their corresponding best-fit rates for 12 of the 17 arrays for which both rates are available in the original 10-year measurements described by Burford and Harsh (1980), suggesting that the alignment array endpoint rates record distributed shearing that is not captured by the best-fit estimates. The highest rates of 30–33 mm/yr are observed on the northwest end of the central creeping segment.

Short-range networks along the creeping segment, surveyed by infrared electronic distance meter, also provide an estimate of fault slip rates by assuming that line-length changes in each network are due to motion parallel to the local fault orientation. Lisowski and Prescott (1981) report a maximum rate of 29 ± 3 mm/yr just north of Slack Canyon and average creep rates of 28 ± 2 mm/yr for much of the central creeping segment.

GPS stations MEE1 and MEE2 span the creeping segment near the Mee Ranch alignment array and provide another independent measure of the behavior of the creeping segment at the 1-km scale. Their relative motion of 28.2 ± 0.5 mm/yr (Fig. 8c), though ~5 mm/yr faster than the 33-year best-fit rate for the Mee Ranch alignment array (Table 1), agrees well with the 28 ± 2 mm/yr rate determined from the short-range Mee Ranch net (Lisowski and Prescott, 1981), also at the 1-km scale.

We suggest that the often-cited 30–33 mm/yr endpoint rates that were reported for four alignment arrays by Burford and Harsh (1980) are outliers at this scale of observation. Endpoint rates for these four arrays are on average 7 ± 4 mm/yr faster than the corresponding best-fit rates. In contrast, the average difference between pairs of endpoint and best-fit rates for the other arrays is only 0.6 ± 2 mm/yr, suggesting that smaller discrepancies between the two rate estimates are more typical. In addition, the three endpoints rates along the northwest central creeping segment (Fig. 9b) are higher than other measures of fault creep at greater distances from the San Andreas fault (Fig. 9c). We propose 28 ± 2 mm/yr for the average creep rate for the central creeping segment at this scale of observation.

Farfield Rates

Measures of fault creep at distances that exceed 1 km come from geodolite measurements, continuous GPS stations, satellite laser ranging, and very long baseline interferometry. These techniques capture discrete and distributed deformation across much of the San Andreas fault system (Fig. 9c).

Geodolites record line-length changes between two stations, approximately 20 km apart, at a high angle to the fault. The average creep rate determined by this method is 32 ± 2 mm/yr (Lisowski and Prescott, 1981). Two anomalously slow rates from geodolite lines between Bitterwater and San Juan Bautista (Fig. 9c) come from monuments that span shorter distances and thus do not capture as much of the total deformation across the fault system. The relative site motion between continuous GPS stations GR8V and QCYN, which span a cross-fault distance of approximately 70 km, is 33.6 ± 1 mm/yr (Fig. 8c). This rate exceeds that determined from

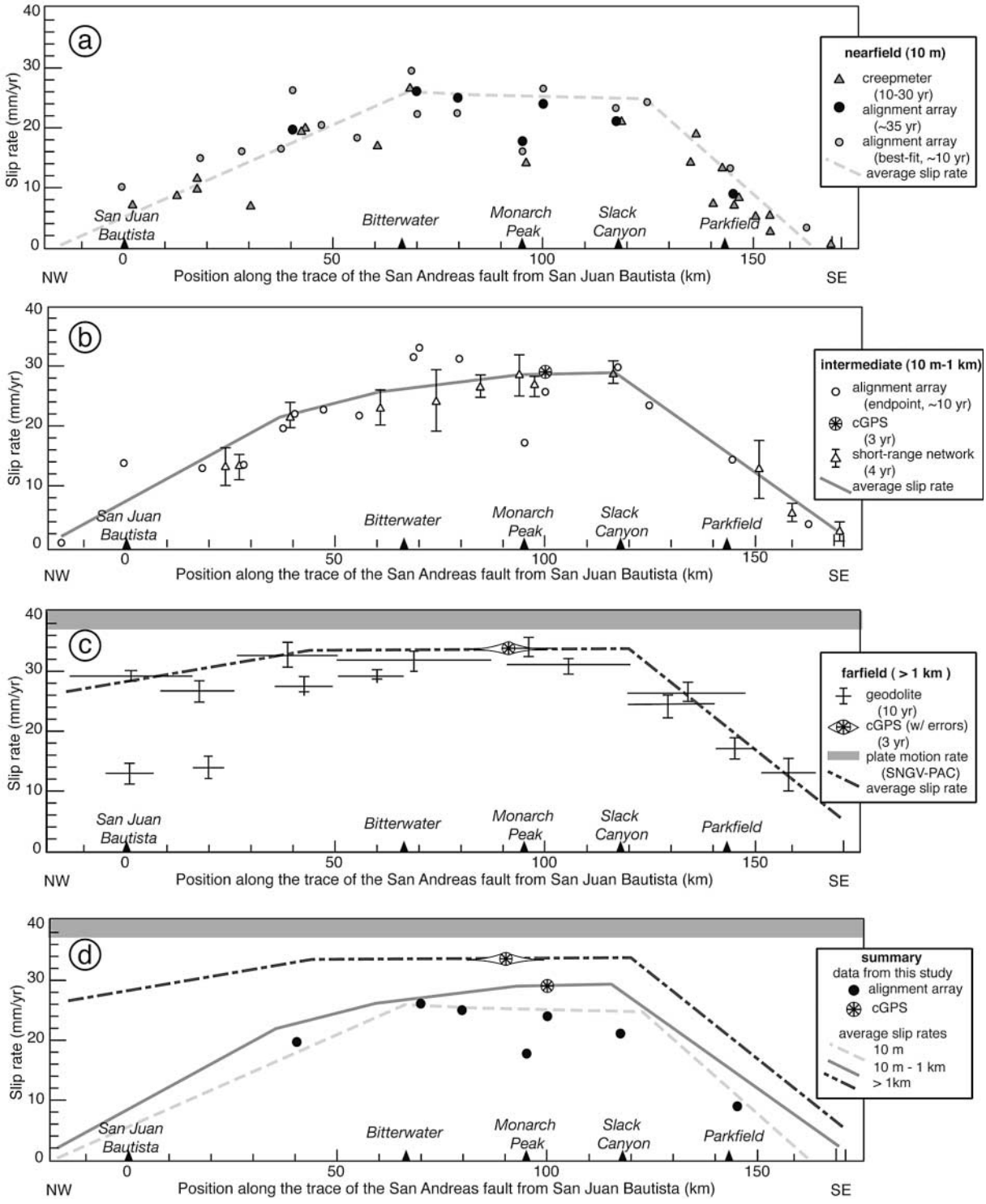

Figure 9. Compilation of fault-parallel deformation rate estimates for the creeping segment at distances of (a) ±10 m, (b) 10m to 1km (c) >1 km from the fault. (d) The data presented in this study are shown with the average deformation rates at each scale of observation. Data sources are as follows: creepmeter data, Schulz *et al.* (1982) and Schulz (1989); 10-year alignment array data, Burford and Harsh (1980); short-range networks and geodolite data, Lisowski and Prescott (1981); 35-year alignment array data and continuous GPS data, Titus *et al.* (2005) and this study; plate motion rate for Sierra Nevada–Great Valley (SNGV) and Pacific (PAC) plates, Argus and Gordon (2001). Modified from Burford and Harsh (1980) and Lisowski and Prescott (1981).

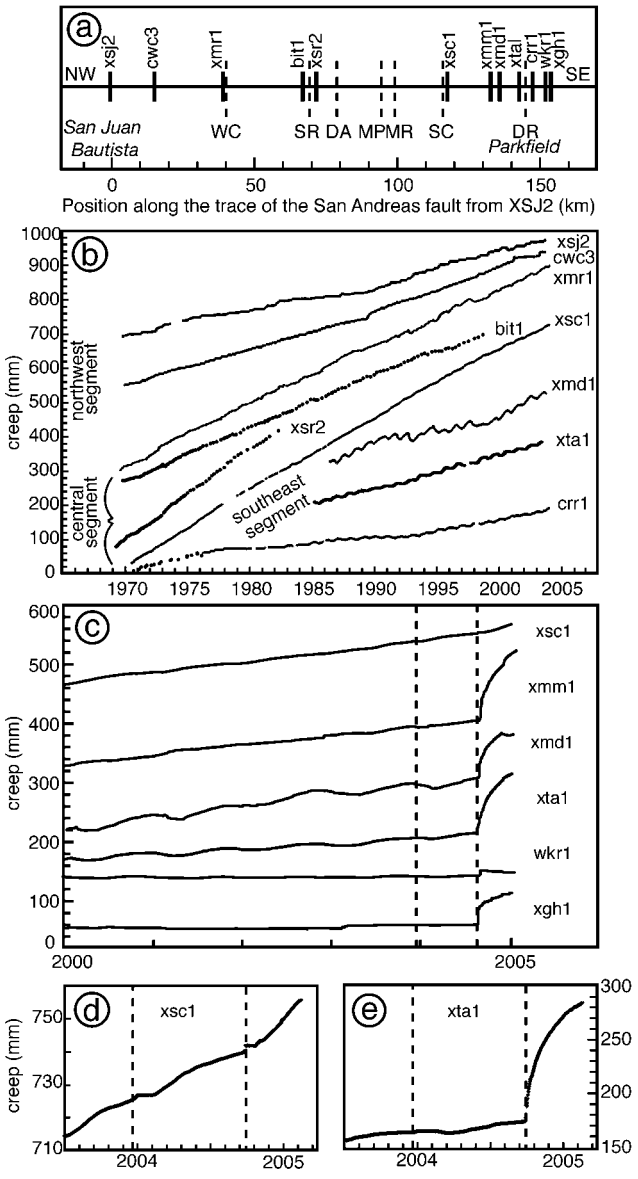

Figure 10. (a) Creepmeter locations (solid lines) from selected sites along the trace of the San Andreas fault shown with alignment array locations (dotted lines, same abbreviations as in Fig. 1). Creepmeter data (b) since 1970, showing long-term trends along the entire creeping segment and (c) since 2000 showing the effects of the San Simeon and Parkfield earthquakes on creepmeters from Slack Canyon (XSC1) and selected creepmeters near Parkfield. Enlargements of creepmeter data at (d) Slack Canyon and (e) Taylor Ranch (XTA1) from mid-2003 to early 2005. Vertical dotted lines in (c), (d), and (e) show the dates of the San Simeon and Parkfield earthquakes.

geodolite lines by ~2 mm/yr, suggesting that additional elastic or permanent deformation accumulates at distances greater than 10–15 km from the fault. The GPS and geodolite data combined suggest an average deformation rate of 33 ± 2 mm/yr for the central creeping segment that includes deformation up to 35 km from the fault.

At the broadest scale, the fault-parallel rate from very long baseline interferometry, satellite laser ranging, and GPS measurements is 39 ± 2 mm/yr for the motion between the Sierra Nevada–Great Valley block and the Pacific plate at the latitude of the Mee Ranch (Argus and Gordon, 2001). Mechanisms by which deformation occurs at distances greater than those sampled by sites GR8V and QCYN are discussed later in the article.

Creeping Segment Response to the Parkfield Earthquake

We resurveyed three alignment arrays along the central and southeast sections of the creeping segment in December 2004 to document the effects of the 28 September 2004 Parkfield earthquake on the creeping segment (Table 1). Relative to the hypocenter of the earthquake, the Durham Ranch. Slack Canyon, and Mee Ranch alignment arrays are located 9 km, 36 km, and 54 km to the northwest, respectively. We compare the results at each location to available creepmeter and continuous GPS data in order to document the spatial effects of the Parkfield earthquake along the creeping segment. For the three alignment arrays, we removed the cumulative displacement of the alignment monuments from long-term creep that occurred at each site between the two surveys, thereby isolating any differential coseismic or postseismic motion that occurred across the alignment arrays within 2 months following the earthquake.

Southeast Segment

As expected, the greatest effects of the Parkfield earthquake are localized near Parkfield along the southeast end of the creeping segment. See Lienkaemper *et al.* (2006) for a detailed discussion of alignment array creep rates near Parkfield. Our observations come from two surveys at the Durham Ranch alignment array (Fig. 11), located 9 km northwest of the epicenter. After correcting for nine months of creep between the two surveys, stations on the northeast side of the San Andreas fault (designated by Sierra Nevada–Great Valley sites in Fig. 11) moved approximately 150 mm toward the southeast parallel to the fault with respect to the alignment monuments southwest of the fault (designated Pacific plate sites in Fig. 11). For comparison, the total fault-parallel displacement for the previous 36 years was approximately 315 ± 30 mm.

The fault-perpendicular displacements for the Durham Ranch alignment sites northeast of the fault are consistent with contraction across the fault that decays in magnitude with distance from the fault (Fig. 11). The Pacific plate monuments exhibited up to 50 mm of vertical motion, significantly greater than the 20 mm documented by Sylvester (1995) for spirit leveling surveys over a 6-year interseismic period in the Parkfield area. Despite the higher level of noise in our estimates of the vertical motion (~10 mm) (Fig. 5) we believe the measured vertical motion is real because up-

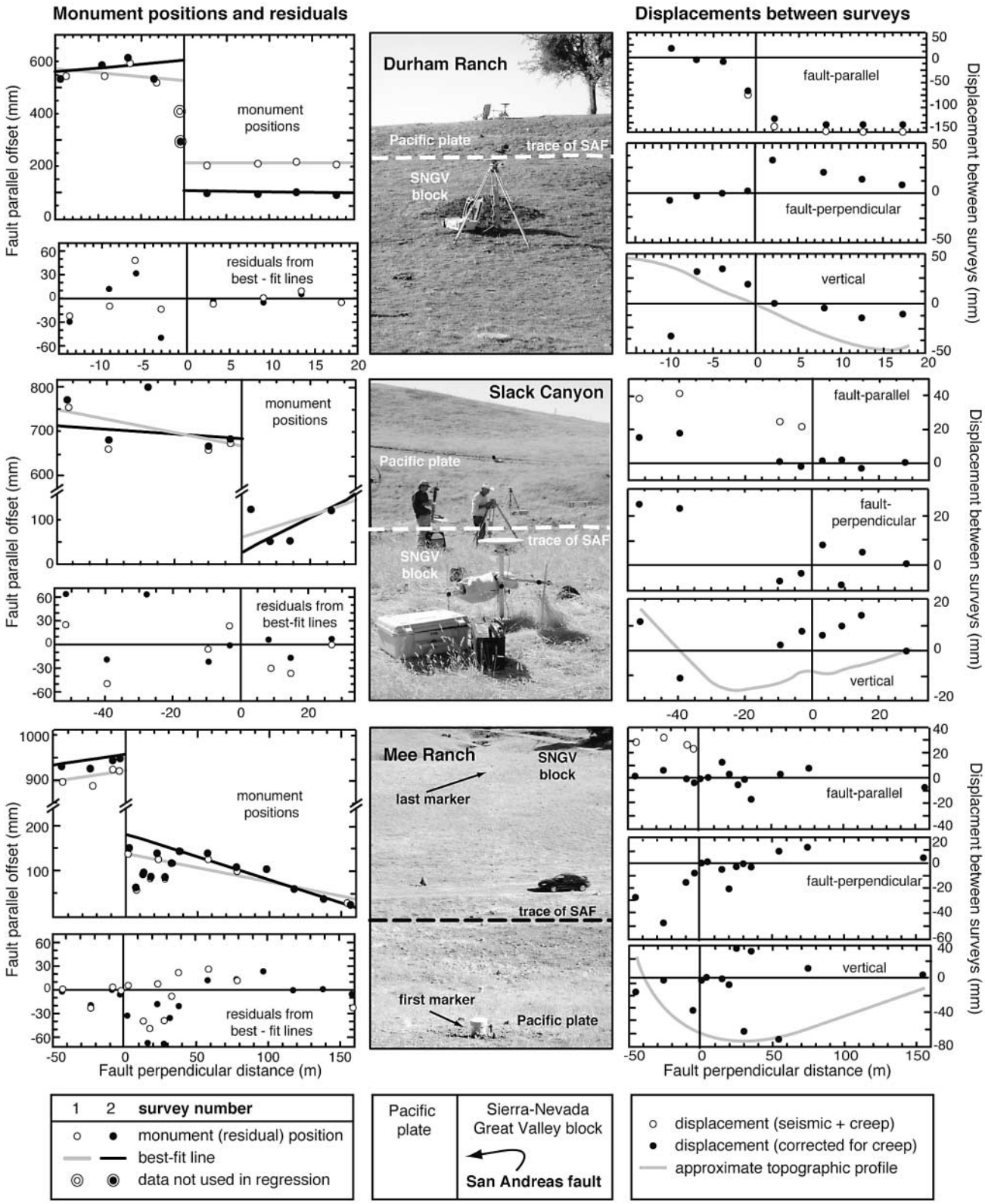

Figure 11. Differential GPS data from two surveys of the Durham Ranch, Slack Canyon, and Mee Ranch alignment arrays. Charts on the left show monument locations and best-fit lines (upper panels) and residuals from those best-fit lines (lower panels). The axes for these charts are the same as in Figure 7, although the vertical and horizontal scales are not uniform. Annotated photographs in the center show each alignment array. Charts on the right show the fault-parallel (upper panel), fault-perpendicular (middle panel), and vertical (lower panel) displacements between our two differential GPS surveys before and after the Parkfield earthquake. Note that the vertical and horizontal scales vary for these plots. White circles in the fault-parallel panel denote the total displacements between surveys, whereas the black circles are creep-corrected displacements based on long-term creep rates from Table 1. The thick gray lines on the vertical displacement panels indicate the local topography, with scales of 6 m, 5 m, and 10 m for the Durham Ranch, Slack Canyon, and Mee Ranch alignment arrays, respectively.

lift is dominantly on the Pacific side of the fault (same as the reference station) and uplift closely mimics the topography (depicted by the curved gray line in the right column of Fig. 11). The measured uplift and topographic profiles are both evidence for a push-up structure crossed by the alignment array.

Measurements from creepmeter XTA1 near the Durham Ranch from the date of the earthquake to the date of our Durham Ranch survey support our results (Fig. 11). Creepmeter XTA1 exhibits 80 ± 5 mm of triggered slip (Fig. 10e) within two months of the earthquake. The difference between offsets recorded at the Durham Ranch alignment array and creepmeter XTA1 could result from a variety of factors, including the latter's 2-km-greater distance from the earthquake epicenter, along-fault variations in the magnitude and/or timing of triggered creep, and incomplete spatial sampling of the full width of the creeping zone by XTA1.

Transition to Central Segment

The Slack Canyon alignment array is located at the transition between the central and southeast sections of the creeping segment and displays more muted effects of the Parkfield earthquake, which was focused 36 km to the southeast. Removal of the fault-parallel creep accumulated between our two surveys does not restore the two northeastmost monuments to their preearthquake positions (Fig. 11), indicating that up to 15 mm of offset was caused by coseismic and postseismic motion.

The same two monuments exhibit significant motion perpendicular to the fault, indicating that both experienced nearly identical displacements in response to the earthquake. Motion during and after the earthquake appears to be displaced northeastward with respect to that recorded in the decades preceding the earthquake (Fig. 7), possibly indicating that motion was focused along a subsidiary fault splay.

Although the vertical displacements are small (<20 mm), downward motion occurs at the lowest topographic point crossed by the alignment array and therefore, like the Durham Ranch alignment array, vertical displacements crudely mimic the topography. This array is situated between two small sag ponds, thus the downward displacements may be consistent with local extension.

Creepmeter data from Slack Canyon (XSC1, Fig. 10) immediately adjacent to the alignment array demonstrate accelerated creep to ~45 mm/yr during the first 5 months after the earthquake, twice its preearthquake rate. The ~8 mm of coseismic and postseismic creep that was recorded at XSC1 between the earthquake and our second alignment array survey is broadly consistent with our GPS-derived offset of 15 mm (Fig. 11).

Central Segment

Repeat surveys of the Mee Ranch alignment array near the center of the central creeping segment indicate no significant effects of the Parkfield earthquake (Figs. 4, 11). Removal of creep between surveys for four Pacific plate monuments (left side) demonstrates no significant motion for two of the four monuments and 4–8 mm of motion for the other two (Fig. 4c), close to the resolution of our differential GPS measurements. The observations are thus consistent with little or no coseismic and postseismic offsets due to the Parkfield earthquake, with a likely upper bound of 5 mm.

Although no creepmeter data are available near the Mee Ranch, the MEE1 and MEE2 GPS stations are located less than 500 m from each end of the alignment array. As is discussed in the previous section, their GPS time series also show no clear evidence for differential coseismic or postseismic motion after the Parkfield earthquake (Fig. 8c). The independent GPS and alignment measurements from the Mee Ranch constitute strong evidence that the Parkfield earthquake did not trigger sympathetic coseismic or postseismic slip along this part of the central creeping segment at a level exceeding several millimeters.

Discussion

The geodetic data described above and summarized in Figure 9d reinforce previously published estimates of along-strike and across-fault variations in deformation rates for the creeping segment of the San Andreas fault. These short-term along-strike and across-fault creep rates are compared with geologic slip rates in the two following sections in order to develop a long-term understanding of deformation in this region.

Long-Term Slip along the San Andreas Fault

Creep rates from creepmeters and best-fit alignment array inversions vary from 21 to 26 mm/yr along the central creeping segment and serve as useful lower bounds on the surficial creep rate within 20 m of the San Andreas fault trace. Since creep occurring at depths of tens to hundreds of meters may propagate to the surface across a somewhat wider zone, as our own and previous measurements clearly indicate is the case at Monarch Peak (Table 1) (Burford and Harsh, 1980; Rymer *et al.*, 1984), a slightly wider definition of the fault zone is useful for constraining surficial creep rates. Based on the consistency of most intermediate distance measurements (Fig. 9b), the simplest interpretation of the data presently available is that the surficial creep rate is 28 ± 2 mm/yr along much or all of the central creeping segment between Bitterwater and Slack Canyon.

Estimates of the fault slip rate over intervals longer than 100 years for the central creeping segment corroborate this interpretation. At Bitterwater, a 95-year old fence surveyed with GPS gives a 22–28 mm/yr slip rate (Swanson *et al.*, 2004) and an offset steam channel yields a rate of 34 mm/yr, assuming that gully formation began in 1885 (Hay *et al.*, 1989). Offset paleostream channels, also at Bitterwater, indicate an average slip rate of ~28 mm/yr for the past 1000

years (Hay *et al.*, 1989). Both the 100-year and 1000-year slip rates agree well with the modern surficial creep rate of 28 mm/yr, suggesting there has been little elastic strain accumulation or release at this site. Microstructures from trenches at Bitterwater also support a lack of rupture of this segment for the past 1000 years (Swanson *et al.*, 2004).

Long-term slip rates on adjacent segments of the fault are higher to the southeast and lower to the northwest than for central creeping segment. A fault trenching study at Wallace Creek 130 km to the southeast determined a 3700-year geologic slip rate of 34 ± 3 mm/yr (Fig. 1) (Sieh and Jahns, 1984). The fault zone geometry at this site is relatively simple and similar to the central creeping segment, with one major fault strand and several subparallel minor faults. At the Melendy Ranch ~25 km northwest of Bitterwater, Perkins *et al.* (1989) found an 800-year slip rate of $22^{+6}/_{-4}$ mm/yr. The agreement of long- and short-term slip rates at this site (e.g., Tables 1 and 2) suggest that there is little strain accumulation on the San Andreas fault. Perkins *et al.* (1989) attribute the slower long-term slip rate at this location to transfer of slip onto the subparallel Paicines fault 3 km northeast of the Melendy Ranch (Fig. 1). There are numerous strands of the San Andreas fault system further northwest near San Francisco, and therefore slip rates on the San Andreas fault in this area are not useful for comparison with those from the creeping segment and the Carrizo Plain.

Accommodating Slip across the San Andreas Fault System

The data presented here also provide constraints on where, though not how, slip is accommodated across the San Andreas fault system. Figure 12 shows two possible models that account for the total 39 mm/yr of transcurrent motion predicted for the Sierra Nevada–Great Valley block and the Pacific plate (Argus and Gordon, 2001). Each model explains the observed increase in slip rates at progressively larger distances from the central creeping segment (Fig. 9) by assuming different deep slip rates. One model (Fig. 12a) assumes that the deep and surficial slip rates are both 28 mm/yr, corresponding to uniform slip with depth. A second model (Fig. 12b) assumes that the deep slip rate matches the 34 mm/yr paleoseismologic slip rate from Wallace Creek (Fig. 1) (Sieh and Jahns, 1984), and that the surficial creep rate is 28 mm/yr. These models represent two end members in an entire spectrum of possible models for the distribution of transcurrent deformation, and each model has different implications for the distribution of seismic hazards in central California, as discussed subsequently.

For the uniform slip model (Fig. 12a), ~11 mm/yr of deformation must occur off the San Andreas fault in order to equal the 39 mm/yr of slip predicted for Pacific plate–Sierra Nevada–Great Valley motion. The observed slip rates increase from 28 mm/yr on the fault to 33 mm/yr at distances of ~30 km (Fig. 9d), and no major known faults are exposed across this distance. We therefore attribute the ~5 mm/yr of slip out to distances of 35 km from the fault to distributed deformation in the fault borderlands. Mapped *en echelon* folds on both sides of the creeping segment may accommodate some of the deformation. These folds are often interpreted to form under conditions involving a component of fault-parallel wrench (transcurrent) deformation (e.g., Harding, 1973; Wilcox *et al.*, 1973; Jamison, 1991; Miller, 1998). The remainder of the plate boundary motion (6 ± 2 mm/yr) may be accommodated on structures farther from the fault such as the Rinconada and San Gregorio–Hosgri faults, as well as structures between the major fault strands. Current slip-rate estimates are 3 ± 2 mm/yr for the Gregorio–Hosgri fault (Working Group on California Earthquake Probabilities, 2003; Hanson *et al.*, 2004) and ~2 mm/yr for the Rinconada fault (Bilham and Bodin, 1992). *En echelon* folds are also present adjacent to the Rinconada fault (Dibblee, 1976).

This model implies that there is no seismic cycle on the creeping segment and, because of the broader distribution of the total plate motion, that there is increased seismic hazard on structures off the main fault strand. The 2003 San Simeon earthquake offers evidence for deformation in the more distal parts of the San Andreas fault system. This model is also supported by the agreement of short- and long-term slip rates (Hay *et al.*, 1989) and the microstructures observed at Bitterwater (Swanson *et al.*, 2004), both of which suggest the central creeping segment has been deforming aseismically for the past 1000 years. An important corollary to the uniform slip model is that the deep slip rate on the creeping segment is different from the 34 mm/yr deep slip rate inferred for Wallace Creek along the Carrizo Plain to the southeast (Sieh and Jahns, 1984).

An alternative end-member model, where the surficial creep rate is 28 mm/yr but the deep slip rate matches the maximum geologic slip rate of 34 mm/yr (Fig. 12b), accounts for the difference in slip rates with depth by assuming there is frictional fault locking at depth causing elastic strain accumulation and release in the crust flanking the fault. In this model, the observed gradual increase in slip rates away from the fault is a consequence of distributed elastic strain. The maximum observed rate of 33 ± 2 mm/yr at sites distant from the fault (Fig. 9c) is equal to the deep fault slip rate. Similar to the uniform slip model (Fig. 12a), the remainder of the transcurrent motion (~6 mm/yr) can be accommodated by slip on other subparallel faults and distributed deformation outside the area sampled by geodolite lines and continuous GPS.

This model implies that earthquakes occasionally rupture the creeping segment, consistent with historical evidence for several **M** 5.5 or greater earthquakes in the area (Toppozada *et al.*, 2002). One advantage of this model is that there is no implied discrepancy between the deep slip rates on the creeping segment and Carrizo plain fault segments. The model, though inconsistent with paleoseismologic evidence from Bitterwater of a long-term 28 mm/yr slip rate for the past 1000 years, could be reconciled with

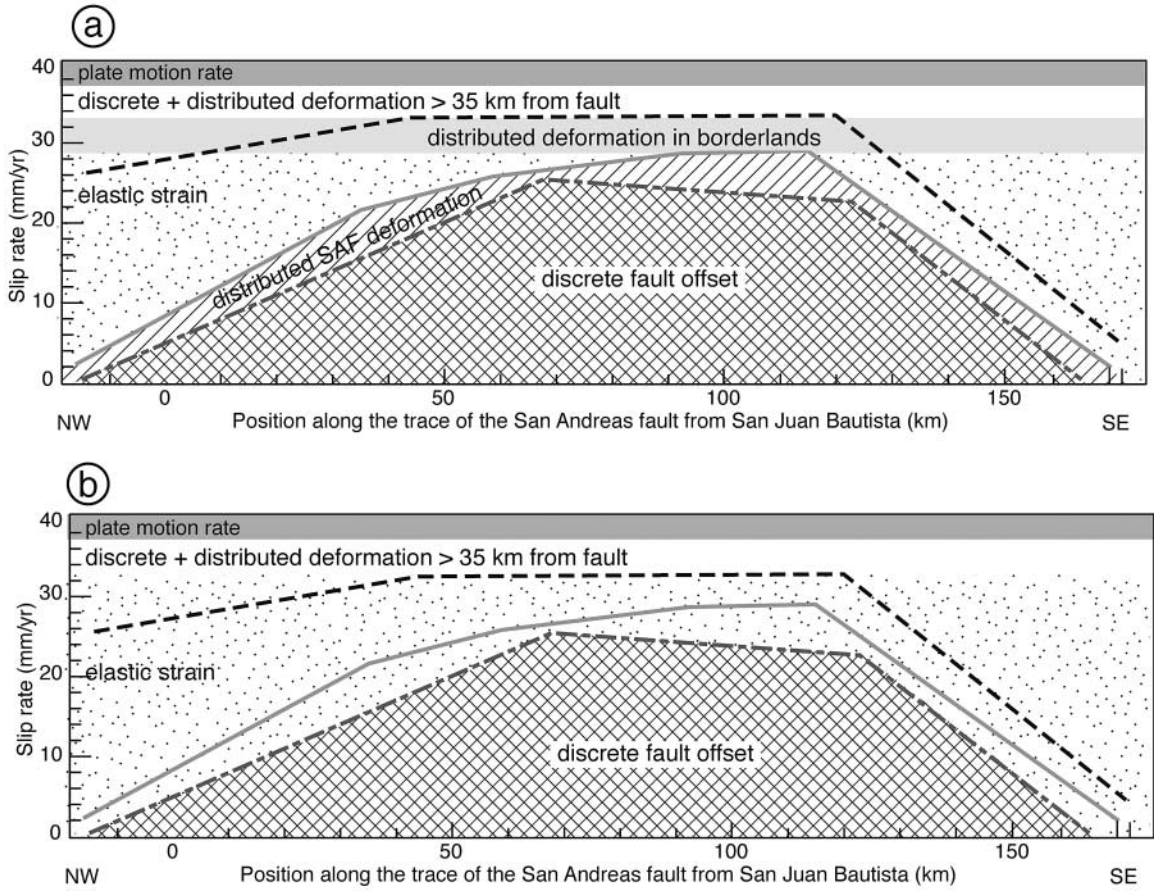

Figure 12. Schematic version of Figure 9d showing two possible models for the accommodation of transcurrent deformation. (a) The deep slip rate is the same as the surficial creep rate. The observed gradient in deformation rates across the central creeping segment is attributed to discrete and distributed offsets on both the San Andreas fault and other structures adjacent to the fault. (b) The deep slip rate is the same as the geologic long-term slip rate. The observed gradient in deformation rates perpendicular to the fault is attributed to elastic strain accumulation on the San Andreas fault, with the remainder accommodated by discrete and distributed deformation on other structures. See text for details.

that observation if some slip along the San Andreas fault has been transferred to the Paicines fault, as proposed by Perkins *et al.* (1989) for the nearby Melendy Ranch.

Implications

Many models of the San Andreas fault incorporate a deep slip rate for the creeping segment based on some of the measurements discussed in the previous section. The rates chosen for these models vary widely, including 23–25 mm/yr (Nadeau and Johnson, 1998; Murray *et al.*, 2001) 26–29 mm/yr (Harris and Segall, 1987; Argus and Gordon, 2001); 30–33 mm/yr (Slawson and Savage, 1983; Jones and Wesnousky, 1992; Ben-Zion *et al.*, 1993), and >33 mm/yr (Simpson *et al.*, 1988; Thatcher and England, 1998; Bokelmann and Kovach, 2003; Horsman and Tikoff, 2005). Further, analysis of data from the same location can yield results consistent with either model presented above. For example, Harris and Segall (1987) determine a deep slip rate for Parkfield of between 25.5–32.7 mm/yr based on 30 years of trilateration data, consistent with both models. Murray *et al.* (2001) use 8 years of GPS data from Parkfield to infer a deep slip rate of 32.6 mm/yr, consistent with the latter model.

Knowing the deep slip rate for the creeping segment is clearly required for a full understanding of how transcurrent deformation is partitioned along and across the San Andreas fault system. The current constraints suggest useful lower and upper bounds of approximately 28 mm/yr and 34 mm/yr for the slip rate on the San Andreas fault in central California. Additional geodetic and geologic data are clearly needed to refine our understanding of and resolve the reasons for the along-strike and across-fault variations of deformation for the San Andreas fault system.

Conclusions

Differential GPS surveys of seven alignment arrays along the creeping segment of the San Andreas fault document 35-year minimum slip rates of 26 mm/yr in the northwest near Bitterwater decreasing to 21 mm/yr in the southeast at Slack Canyon. These rates agree well with 10-year alignment array best-fit rates and rates derived from creepmeters, which sample deformation at the same scale. Our differential GPS methodology for surveying alignment arrays, though less precise than theodolite surveys, works well for estimating long-term discrete offsets along the creeping segment.

In addition, surveys of three alignment arrays both before and after the 2004 Parkfield earthquake were used to document horizontal and vertical displacements due to coseismic and postseismic motion at these arrays. Horizontal displacements of 150 mm, 15 mm, and <5 mm were determined for alignment arrays at distances of 9, 36, and 54 km from the earthquake epicenter, respectively. The latter two sites are located along the apex of the creeping segment, where measured slip rates are the highest. Our observations thus indicate that any coseismic or postseismic effects associated with the Parkfield earthquake were localized near Parkfield and that motion along the central creeping segment was affected little or not at all.

Four continuous GPS stations operating since 2003 provide creep rate estimates of 28.2 ± 0.5 and 33.6 ± 1 mm/yr spanning the central creeping segment at respective distances of ± 0.5 km and ± 35 km from the fault. The 2003 San Simeon earthquake did not trigger any apparent changes in secular GPS rates for the four sites flanking the creeping site, nor were measurable coseismic or postseismic responses observed for the 2004 Parkfield earthquake. Our GPS measurements support results from our alignment array surveys, which indicate there was little response of the central creeping segment to the Parkfield earthquake.

Integrating our creep rate estimates from alignment arrays and continuous GPS with other slip rate estimates at different scales demonstrates that faster slip rates are observed at greater distances from the fault. This pattern may reflect the effects of distributed deformation adjacent to the San Andreas fault, elastic strain accumulation along the creeping segment due to frictional coupling at depth, or some combination thereof.

Acknowledgments

We are grateful to Bill Eade, Pete Duncan, Phil Martin, Bill Petrovich, and Bill Whitney for access to critical localities. For their assistance in the field, we thank Joshua Davis, Neal Lord, Skylar Primm, Bill Unger, and especially Scott Giorgis. Scott Giorgis and Eric Horsman provided thoughtful and critical reviews on earlier versions of this manuscript, and we thank John Langbein, Ramon Arrowsmith, and an anonymous reviewer for their suggestions that greatly improved the clarity of this manuscript. John Langbein was also extremely helpful locating the original alignment array data and Andy Snyder helped us gain access to several alignment arrays. This material is based upon work supported under a National Science Foundation Graduate Research Fellowship (S.J. Titus) and supported by NSF-EAR0208038.

References

Allen, C. R. (1968). The tectonic environments of seismically active and inactive areas along the San Andreas fault system, in *Proc. of the Conference on Geologic Problems of the San Andreas Fault System*, W. R. Dickinson and A. Grantz (Editors), *Stanford Univ. Publ. Geol. Sci.* **11,** 70–82.

Altamimi, Z., P. Sillard, and C. Boucher (2002). ITRF2000: a new release of the International Terrestrial Reference Frame for earth science applications, *J. Geophys. Res.* **107,** 2214, doi 10.1029/2001JB000561.

Argus, D. F., and R. G. Gordon (2001). Present tectonic motion across the Coast Ranges and San Andreas fault system in central California, *Geol. Soc. Am. Bull.* **113,** 1580–1592.

Baker, B. (1993). Deformation across the San Andreas fault near Parkfield, California, *M.S. Thesis*, University of Wyoming, Laramie, 117 pp.

Ben-Zion, Y., J. R. Rice, and R. Dmowska (1993). Interaction of the San Andreas fault creeping segment with adjacent great rupture zones and earthquake recurrence at Parkfield, *J. Geophys. Res.* **98,** 2135–2144.

Bilham, P., and P. Bodin (1992). Fault zone connectivity: slip rates on faults in the San Francisco Bay, California, *Science* **258,** 281–284.

Bokelmann, G. H. R., and R. L. Kovach (2003). Long-term creep-rate changes and their causes, *Geophys. Res. Lett.* **30,** doi 10.1029/2003GL017012.

Brown, R. D., Jr. (1970). Map showing recently active breaks along the San Andreas and related faults between the northern Gabilan Range and Cholame Valley, California, U.S. Geol. Surv. Misc. Geol Invest. Series Map 1-575, scale 1:62,000.

Brown, R. D., Jr., and R. E. Wallace (1968). Current and historic fault movement along the San Andreas fault between Paicines and Camp Dix, California, in *Proc. of the Conference on Geologic Problems of the San Andreas Fault System, Stanford Univ. Publ. Geol. Sci.* **11,** 22–39.

Burford, R. O., and P. W. Harsh (1980). Slip on the San Andreas fault in central California from alinement array surveys, *Bull. Seism. Soc. Am.* **70,** 1233–1261.

Dibblee, T. W., Jr. (1976). The Rinconada and related faults in the southern Coast Ranges, California and their tectonic significance, *U.S. Geol. Surv. Profess. Pap. 981*, 55 pp.

Dixon, T., M. Miller, F. Farina, H. Wang, and D. Johnson (2000). Present-day motion of the Sierra Nevada block and some tectonic implications for the Basin and Range Province, North American Cordillera, *Tectonics* **19,** 1–24.

Galehouse, J. S., and J. J. Lienkaemper (2003). Inferences drawn from two decades of alinement array measurements of creep on faults in the San Francisco Bay region, *Bull. Seism. Soc. Am.* **93,** 2415–2433.

Genrich, J. F., and Y. Bock (1992). Rapid resolution of crustal motion at short ranges with the Global Positioning System, *J. Geophys. Res.* **97,** 3261–3269.

Hanson, K. L., W. R. Lettis, M. K. McLaren, W. U. Savage, and N. T. Hall (2004). Style and rate of Quaternary deformation of the Hosgri fault zone, offshore southern California, *U.S. Geol. Surv. Bull. 1995-BB*, 33 pp.

Harding, T. P. (1973). Newport-Inglewood Trend, California: an example of wrenching style of deformation, *Am. Assoc. Petrol. Geol. Bull.* **57,** 97–116.

Harris, R. A., and P. Segall (1987). Detection of a locked zone at depth on the Parkfield, California segment of the San Andreas fault, *J. Geophys. Res.* **92,** 7945–7962.

Hay, E. A., N. T. Hall, and W. R. Cotton (1989). Rapid creep on the San Andreas fault at Bitterwater Valley, in *Sedimentation and Tectonics of Western North America, The San Andreas Transform Belt: Field Trips for the 28th International Geological Congress*, A. G. Sylvester and J. C. Crowell (Editors), Vol. 2, 36–39.

Heflin, M., W. Bertiger, G. Blewitt, A. Freedman, K. Hurst, S. Lichten, U. Lindqwister, Y. Vigue, F. Webb, T. Yunck, and J. Zumberge (1992). Global geodesy using GPS without fiducial sites, *Geophys. Res. Lett.* **19,** 131–134.

Horsman, E., and B. Tikoff (2005). Quantifying simultaneous discrete and distributed deformation, *J. Struct. Geol.* **27,** 1168–1189.

Jamison, W. R. (1991). Kinematics of compressional fold development in convergent wrench terranes, *Tectonophysics* **190,** 209–232.

Jones, C. H., and S. G. Wesnousky (1992). Variations in strength and slip rate along the San Andreas fault system, *Science* **256,** 83–86.

Langbein, J., and H. Johnson (1997). Correlated errors in geodetic time series: implication for time-dependent deformation, *J. Geophys. Res.* **102,** 592–604.

Lienkaemper, J. J., B. Baker, and F. S. McFarland (2006). Surface slip associated with the 2004 Parkfield, California, earthquake measured on alinement arrays, *Bull. Seism. Soc. Am.* **96,** no. 4B, S239–S249.

Lisowski, M., and W. H. Prescott (1981). Short-range distance measurements along the San Andreas fault system in central California, 1975 to 1979, *Bull. Seism. Soc. Am.* **71,** 1607–1624.

Marquez-Azua, B., and C. DeMets (2003). Crustal velocity field of Mexico from continuous GPS measurements, 1993 to June 2001: implications for the neotectonics of Mexico, *J. Geophys. Res.* **108,** doi 10.1029/2002JB002241.

Miller, D. D. (1998). Distributed shear, rotation, and partitioned strain along the San Andreas fault, central California, *Geology* **26,** 867–870.

Murray, J. R., P. Segall, P. Cervelli, W. H. Prescott, and J. L. Svarc (2001). Inversion of GPS data for spatially variable slip-rate on the San Andreas fault near Parkfield, California, *Geophys. Res. Lett.* **28,** 359–362.

Nadeau, R. M., and L. R. Johnson (1998). Seismological studies at Parkfield VI: moment release rates and estimates of source parameters for small repeating earthquakes, *Bull. Seism. Soc. Am.* **88,** 790–814.

Perkins, J. A., J. D. Sims, and S. S. Sturgess (1989). Late Holocene movement along the San Andreas fault at Melendy Ranch: implications for the distribution of fault slip in central California, *J. Geophys. Res.* **94,** 10,217–10,230.

Roeloffs, E. A. (2001). Creep rate changes at Parkfield, California 1966–1999: season, precipitation induced, and tectonic, *J. Geophys. Res.* **106,** 16,525–16,547.

Rymer, M. J., M. Lisowski, and R. O. Burford (1984). Structural explanation for low creep rates on the San Andreas fault near Monarch Peak, central California, *Bull. Seism. Soc. Am.* **74,** 925–931.

Schulz, S. S. (1989). Catalog of creepmeter measurement in California from 1966 through 1988, *U.S. Geol. Surv. Open-File Rept. 89-065.*

Schulz, S. S., G. M. Mavko, R. O. Burford, and W. D. Stuart (1982). Long-term fault creep observations in central California, *J. Geophys. Res.* **87,** 6977–6982.

Sieh, K. E., and R. H. Jahns (1984). Holocene activity of the San Andreas fault at Wallace Creek, California, *Geol. Soc. Am. Bull.* **95,** 883–896.

Simpson, R. W., S. S. Schulz, L. D. Dietz, and R. O. Burford (1988). The response of creeping parts of the San Andreas fault to earthquakes on nearby faults: two examples, *Pure Appl. Geophys.* **126,** 665–685.

Slawson, W. F., and J. C. Savage (1983). Deformation near the junction of the creeping and locked segments of the San Andreas fault, Cholame Valley, California (1970–1980), *Bull. Seism. Soc. Am.* **73,** 1407–1414.

Swanson, K. R., S. M. Cashman, and J. N. Baldwin (2004). Macro- and micro-deformation features of the creeping strand of the San Andreas fault and evidence for changes in historic creep rate, Flook Ranch, Bitterwater Valley, California (abstract), *EOS Trans. AGU* G11A-0764.

Sylvester, A. G. (1995). Nearfield vertical displacement in the creeping segment of the San Andreas fault, central California, 1975 to 1994, *Tectonophysics* **247,** 25–47.

Thatcher, W., and P. C. England (1998). Ductile shear zones beneath strike-slip faults: implications for the thermomechanics of the San Andreas fault zone, *J. Geophys. Res.* **103,** 891–905.

Titus, S. J., C. DeMets, and B. Tikoff (2005). New slip rate estimates for the creeping segment of the San Andreas fault, *Geology* **33,** 205–208.

Tocher, D. (1960). Creep on the San Andreas fault—creep rate and related measurements at Vineyard, California, *Bull. Seism. Soc. Am.* **50,** 396–404.

Toppozada, T. R., D. M. Branum, M. S. Reichle, and C. L. Hallstrom (2002). San Andreas fault zone, California: $M \geq 5.5$ earthquake history, *Bull. Seism. Soc. Am.* **92,** 2555–2601.

Wilcox, R. E., T. P. Harding, and D. R. Seely (1973). Basic wrench tectonics, *Am. Assoc. Petrol. Geol. Bull.* **57,** 74–96.

Working Group on California Earthquake Probabilities (2003). Earthquake probabilities in the San Francisco Bay Region: 2000–2040, *U.S. Geol. Surv. Open-File Rept. 03-214*, 235 pp.

Zumberge, J. F., M. B. Heflin, D. C. Jefferson, M. M. Watkins, and F. H. Webb (1997). Precise point positioning for the efficient and robust analysis of GPS data from large networks, *J. Geophys. Res.* **102,** 5005–5017.

Department of Geology and Geophysics
University of Wisconsin
Madison, Wisconsin 53706

Manuscript received 16 September 2005.